Wear 496-497 (2022) 204301

Contents lists available at ScienceDirect

Wear

journal homepage: www.elsevier.com/locate/wear

Formation of nanostructured surface layer, the white layer, through solid particles impingement during slurry erosion in a martensitic medium-carbon steel

V. Javaheri [a,*], S. Sadeghpour [a], P. Karjalainen [a], M. Lindroos [b], O. Haiko [a], N. Sarmadi [c], S. Pallaspuro [a], K. Valtonen [d], F. Pahlevani [c], A. Laukkanen [b], J. Kömi [a]

[a] Materials and Mechanical Engineering, Centre for Advanced Steels Research, University of Oulu, Finland
[b] Integrated Computational Materials Engineering, VTT Technical Research Centre of Finland, Espoo, Finland
[c] Centre for Sustainable Materials Research and Technology, SMaRT@UNSW, School of Materials Science and Engineering, UNSW, Sydney, Australia
[d] Tampere Wear Center, Materials Science and Environmental Engineering, Faculty of Engineering and Natural Sciences, Tampere University, Finland

ARTICLE INFO

Keywords:
White layer
Martensitic steel
Slurry erosion
Nanocrystalline structure
Cell formation
Martensite deformation
Nanohardness

ABSTRACT

The extremely altered topmost surface layer, known as the white layer, formed in a medium-carbon low-alloy steel as result of impacts by angular 10–12 mm granite particles during the slurry erosion process is comprehensively investigated. For this purpose, the characteristics, morphology, and formation mechanism of this white layer are described based on the microstructural observations using optical, scanning and transmission electron microscopies as well as nanoindentation hardness measurements and modelling of surface deformation. The white layer exhibits a nanocrystalline structure consisting of ultrafine grains with an average size of 200 nm. It has a nanohardness level of around 10.1 GPa, considerably higher than that of untempered martensitic bulk material (5.7 GPa) achieved by an induction hardening treatment. The results showed that during the high-speed slurry erosion process, solid particle impacts brought forth conditions of high strain, high strain rate, and multi-directional strain paths. This promoted formation of a cell-type structure at first and later, after increasing the number of impacts, development of subgrains following by subgrain rotation and eventually formation of a nanocrystalline structure with ultra-high hardness. The model confirmed that high strain conditions - much higher than required for the onset of plastic deformation - can be achieved on the surface resulting in severe microstructural and property changes during the slurry erosion test.

1. Introduction

Steel that has been heavily strained or subjected to intense impact deformation frequently exhibits considerable surface deformation and structural changes in its outermost layer and surrounding sub-surface volume. It is widely reported that a thin, hard, and brittle surface layer can form during some heavy fabrication processes of hardened steels, such as machining [1], grinding [2,3], and hard turning [4–7]. This layer, which is generally known as "white layer (WL)" [8,9], forms due to the significant changes in the structure of the surface and near the surface regions. A similar surface layer has been also reported to be formed on the worn steel surface under high stress abrasion during certain intensive wear processes, such as slurry erosion [10,11] or impact wear [12,13]. This severely deformed superficial layer exhibits unusual and essentially different physical and mechanical properties than those of the bulk material (unaltered region). For example, higher hardness, enhanced tribological properties, and different stress-strain behavior [14]. The term "white layer" originated from the featureless structure of the layer under optical microscopy where it appears white and flawless. So that WL resembles a non-etched or very etch-resistant phase, even after long exposure to the chemical attack by metallography etchants that are generally used for revealing the microstructure. However, the layer often looks like a very fine-structured substrate under scanning electron microscopy. It is worth noting that although WL is the most common term, also several other terms have been proposed to define this superficial structure in various applications [15–18].

Typically, the estimated thickness of WL is in the range of 5–25 μm. The hardness of the layer is found to be significantly higher than that of a

* Corresponding author.
E-mail address: vahid.javaheri@oulu.fi (V. Javaheri).

https://doi.org/10.1016/j.wear.2022.204301
Received 18 November 2021; Received in revised form 11 January 2022; Accepted 18 February 2022
Available online 22 February 2022

hard and fine-grained untempered martensite having the same carbon content [1,19]. When it comes to grain size, ultra-fine grain ranges of a few hundred nanometers to a few micrometers have been reported for the WL [20,21]. In a few wear-related investigations [21–23], strain hardening and grain refinement induced by plastic deformation have been proposed to be the dominant factor enhancing the properties of this layer.

However, there has been no explicit and conclusive study providing sufficient evidence to fully explain the structure and formation mechanism of the WL. During the above-mentioned fabrication processes where the surface temperature increases significantly (sometimes even rises above the austenitizing temperature [1,5]), the WL is explained to be formed mainly by frictional heating followed by quenching because of the colder massive sublayer (bulk material) as well as by contact stresses in service. Hence, the surface layer in those processes is generally referred to as an untempered martensite structure [14,24]. In these cases, the WL consists of a large amount of (retained) austenite. For example, an austenite fraction of about 30% has been reported to be obtained after a hard turning process in a martensitic high carbon-chromium AISI 52100 steel [6]. Hence, Chou and Evans [6] proposed that the WL forms through a thermo-mechanical mechanism where it seems to be dominantly developed by a thermal mechanism involving phase transformation but activated by plastic strain. A large amount of accumulated plastic strain as a result of severe deformation along with the elevated temperature prevailing in the surface area of the deformation zone could also trigger dynamic recrystallization [1]. Hosseini and Klement [5] reported that during hard turning of AISI 52100 bearing steel the thermally induced WL formation is initiated by the severe plastic deformation and then it is continued and controlled by the dynamic recovery and later by the dynamic recrystallization when the temperature is above the dynamic recrystallization onset temperature. A similar observation has been reported by Hossain et al. [24] for a high carbon martensitic steel that was subjected to impact loading by balls. They proposed that a combination of phase transformation due to the heat generated during severe plastic deformation caused by impacts together with strain hardening, and grain refinement led to the development of a hybrid structure with a much higher hardness value (about 20–40% higher than the bulk).

In the case of slurry erosion, the situation is somehow different than in those above-mentioned processes. The overall surface temperature cannot rise that high, as in each impingement the contact time between the erosive solid particles and the target surface is extremely short. Moreover, no phase transformation of martensite to austenite during the slurry erosion process has been reported yet. Thus, the WL formation during slurry erosion can be assumed to be similar to those layers formed superficially during cold deformation or severe plastic deformation at temperatures below 50% of the material melting point. This assumption is based on the nature of the slurry erosion process and parameters involved as well as microstructural features (grain size, morphology) observed in some previous studies [20,25]. In several severe plastic deformation-based studies using various deformation techniques [17, 26,27], especially surface mechanical attrition treatment [28], it has been shown that efficient grain refinement down to a nanoscale could occur due to contact loading and continuous plastic deformation. However, this strain-induced microstructure refinement to a (sub) micron and even to nanometer-scale has been mainly reported for the FCC materials with higher deformability compared to those with the BCC crystal structure [29]. Sakai et al. [21] proposed that extreme grain refinement during severe plastic deformation process in FCC materials like pure copper and aluminum alloy occurs by the formation of new grains with high-angle grain boundaries which are developed gradually by increasing the misorientation of many mutually crossing microshear of kink bands. Tao et al. [30] showed that a nanocrystalline surface can be fabricated during surface mechanical attrition treatment of pure BCC iron under the following mechanism: (i) shear band formation in the initial deformation stage, (ii) dislocation activities and movements, and (iii) nanosized grain formation by a local change of grain orientation and thermally-induced nanocrystallization.

Although the tribological WL formed by repetitive impacts of solid particles on the material surface during the slurry erosion shows some similarity with that observed during severe plastic deformation processes and although nanocrystalline structures have been extensively investigated over the past few decades, still the question remains: can solid particle impacts during slurry erosion generate such a high strain required for the nanocrystalline structure formation? Strain accumulation might be limited particularly in the case of medium-carbon steels possessing martensitic microstructure with low deformability, which are commonly utilized in wear-resistant applications. On the other side, though martensitic steels generally exhibit quite limited deformation capability, even high-hardness martensitic steels have been demonstrated to exhibit surface deformation during severe abrasive wear [31, 32]. To date, the structure of this WL caused by severe high-stress slurry erosion process has not been investigated yet and understanding of the formation mechanism still remains to be somewhat mysterious in the field of wear. Therefore, the present work aims at addressing the above-mentioned deficiencies by a better exploration of the microstructure of this layer, which has been created under a harsh high-speed slurry erosion environment. For this purpose, the surface grain refinement and its mechanism during the slurry erosion phenomenon are described in detail based on microstructural examinations.

2. Material and experimental procedures

Material. A medium-carbon low-alloy steel microalloyed with niobium was investigated in this work. The material composition in mass-percentage was **0.40 C, 0.19 Si, 0.24 Mn, 0.92 Cr, 0.012 Nb**. The composition of the studied steel was designed by the authors as a potential new slurry pipeline material. More details on the composition design and material properties, especially the temperature-dependent properties such as specific heat, thermal conductivity and density can be found in the previous publications [33–35].

The steel was melted and cast using a vacuum induction furnace to ensure a low impurity level [36]. Then, a hot-rolling was carried out to a thickness reduction by 80% [37]. Afterward, cylindrical bar samples were prepared from an as-rolled 10-mm thick sheet. A through-hardening induction treatment was used to achieve a fully martensitic microstructure as well as to increase the hardness of the sample through the whole thickness [35]. The bulk average prior austenite grain size and martensite block size were about 10 ± 2 μm and 2.5 ± 0.5 μm, respectively.

Slurry erosion wear tests. After induction hardening, the cylindrical bar sample with a diameter of 9.5 mm and a total length of 85 mm was subjected to a slurry-erosive condition in a pin-mill type of high-speed slurry-pot test rig [38]. As illustrated in Fig. 1(a), the test rig consists of a cylindrical pot with a diameter of 273 mm and a rotating main shaft with the mounted sample holders at three different levels. The pot was filled with slurry which consisted of a mixture of 10 L of water and 2 kg of crushed and sieved Kuru granite particles with a particle size range of 10–12 mm. The average hardness value of the granite particles was about 1000 HV. The test was performed at 1500 rpm for 180 min. High slurry speed and large erosive particles were used in this test, to simulate realistic slurry transportation conditions. To decrease the effect of particle degradation, after a time interval of 30 min, the slurry was refilled with a fresh one and the level of the samples was swapped. During the test, the pot was cooled with a surrounded copper coil cooling system. The average erosion rate for the studied sample under the chosen test conditions was about 0.009 g/min. However, the slurry erosion performance results of the studied material have been presented comprehensively in previous work [25] and it is not the topic of this paper.

Microstructural characterization. After the slurry erosion testing, microstructural features of the eroded surface (cross-sections) were

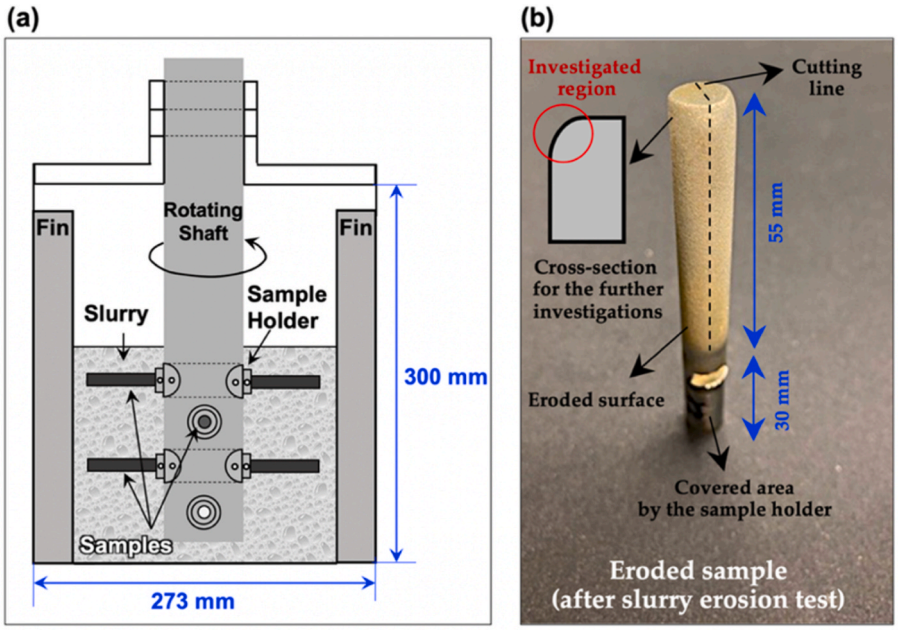

Fig. 1. a) The high-speed slurry-pot test rig set up. b) The sample appearance after the slurry erosion test along with the highlighted selected area for further investigation on the top-left.

examined using a light optical and a laser scanning confocal microscope (LSCM, VK-X200, Keyence Ltd.), a field emission scanning electron microscope (FESEM, Zeiss Sigma) equipped with an electron backscatter diffraction (EBSD) unit, and a scanning transmission electron microscope (STEM, JEOL JEM-2200FS STEM/EFTEM). LSCM sample preparation consisted of cross-sectioning, grinding, and mechanical polishing with 1 μm grade diamond paste followed by Nital etching (2%) to reveal the microstructure. FESEM-EBSD examination was performed on the same sample but without etching and after one more chemical polishing step and surface nickel coating. EBSD mappings were recorded using an acceleration voltage of 15 kV and a working distance of 15 mm with a step size of 0.05 μm. The EDAX-TSL software was employed to post-processing the EBSD data and to study the inverse pole figure orientation maps of the microstructure and relative global orientation of grains. The examined region for both EBSD and TEM investigation was the tip of the samples, which was heavily damaged during the erosion, as highlighted in Fig. 1(b).

To perform a detailed investigation of the eroded surface, especially the superficial WL, and the regions near the surface, the microstructure was characterized using a 200-kV energy-filtered scanning transmission electron microscope (EFTEM/STEM). Thin foils were prepared by focused ion beam (FIB) milling and lifted out using an Omniprobe nano manipulator within the dual-beam workstation. An ion beam current of 9 nA was used to mill a wall of material, which was then lifted onto a copper TEM grid. It was then further thinned to a thickness of about 500 nm with a low ion current (0.26 nA) to eliminate the main part of the ion damage caused by the initial milling process. The surfaces of samples were coated with Pt film before FIB milling to avoid damage to the surface from the incident Ga + ions. Two FIB samples were lifted out to be examined during TEM studies: one sample parallel to the surface and along to the deformation direction, which was consisted of only the WL to study the structure of this layer itself, and another sample perpendicularly to the surface containing mainly the bulk (untouched) but also a part of the WL to study the microstructure evolution in the thickness direction. The positions of these two samples are illustrated in Fig. 2, where A is oblique to the eroded surface and B is parallel to the surface.

Hardness measurements. The hardness of the samples was measured by a CSM Instruments MHT-Z-AE Vickers microhardness tester with 0.1 N load as well as a nanoindentation system in load-control mode at a constant loading rate of 2 mN min^{-1} up to a maximum load of 2 mN. A Hysitron triboindenter with a Berkovich tip was used for all the measurements. The angle between the indenter centerline and the three faces was 65.3°.

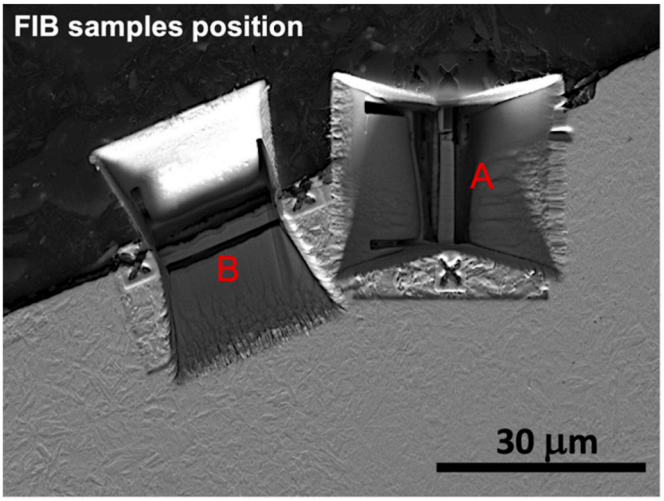

Fig. 2. The position of TEM foils prepared by FIB technique from the regions that contain the bulk material and white layer (A) and only the white layer (B).

Surface deformation modeling. A macroscale impact model was established using the Abaqus Explicit finite element software as described in Fig. 3(a, d). A steel plate representing the target samples is impacted with rock particles that have a rough surface. A plate shape is chosen to simplify the impact conditions in the simulations instead of the cylindrical-shaped samples. Up to five rocks were impacted to the steel surface to evaluate the severity of plastic deformation conditions on the initially undeformed steel plate.

The initial impact velocity of the particle was assigned to 13 m/s equal to the speed of the sample tip during the slurry erosion pot test. Accordingly, the initial size of the rock particles generally varied between 10 and 12 mm (diameter) depending on the measured location of the rock shape. Fig. 3(b) illustrates the applied mesh for the steel part.

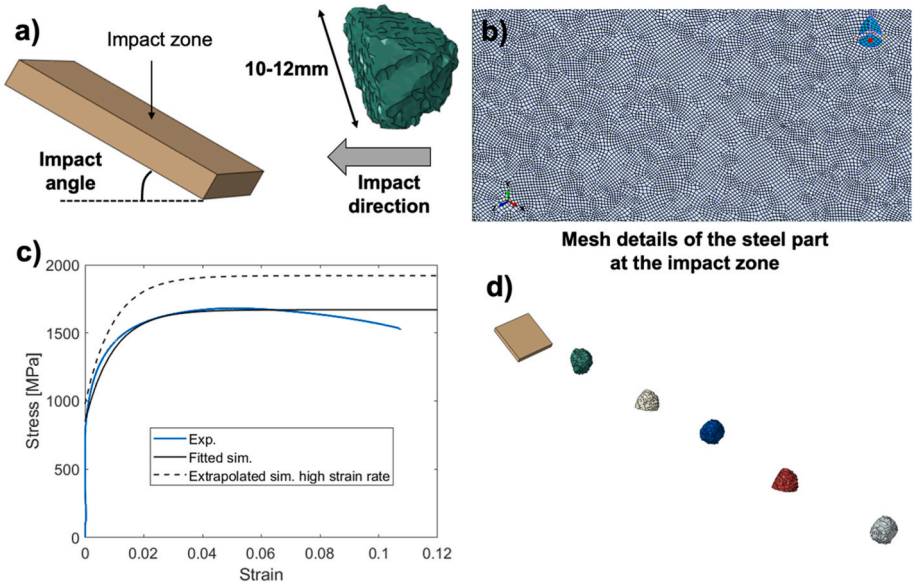

Fig. 3. a) The oblique-angle impact model assembly with rough rocks impacting steel surface, b) mesh details for the analyzed steel part, c) stress-strain behavior for the elasto-plastic model with low strain rate condition (0.008 s^{-1}) and extrapolated high strain rate behavior (4000 s^{-1}), d) five rocks impact assembly.

For computational efficiency, the mesh size was set to be between 20 and 25 μm in-plane direction. The displacements at the bottom of the steel plate were fixed (U1=U2=U3= 0). The size of the impact craters is small compared to the total edge length of the steel plate, so that the displacements at the edges were left free. An impact angle of 30° was used in the simulations. The angle varies in the real test procedure; but this oblique angle has been chosen to analyze surface region plasticity and providing a rough idea about surface deformation. The aim of this modelling is not to provide the whole picture of the slurry erosion process or even to achieve a sufficient resolution of the plastic strain distribution through the target material but to give an example of surface severe plastic deformation under one of the probable conditions during a real test.

The rock particles were treated as isotropic elastic (E =50 GPa, ν = *0.25*) and fracture of the rocks was omitted for simplicity. Steel material was considered as elastoplastic using the J2-plasticity model of Abaqus with the built-in procedure to integrate plastic strain accumulation by the strain rate dependent stress-strain curve inputs Fig. 3(c). Therefore, only isotropic hardening was considered. Stress-strain behavior was defined in quasi-static conditions by fitting to the experimental results. High strain rate behavior was extrapolated in the view of high strain rate behavior of high strength martensitic wear resistant steels in Lindroos et al. [39]. Accordingly, the strain rate sensitivity of similar kinds of martensitic steels is low. Therefore, an approximately 15% increase was assumed in flow stress at a high strain rate condition (4000 s^{-1}) in the transition from the measured quasi-static strain rate condition of 0.008 s^{-1}.

3. Results and discussion

Characterization and structure of white layer. An optical micrograph of the cross-sectioned eroded surface indicating the formation of WL is presented in Fig. 4(a). The WL generated in this sample had a thickness of approximately 5–10 μm. Due to the impingements of large

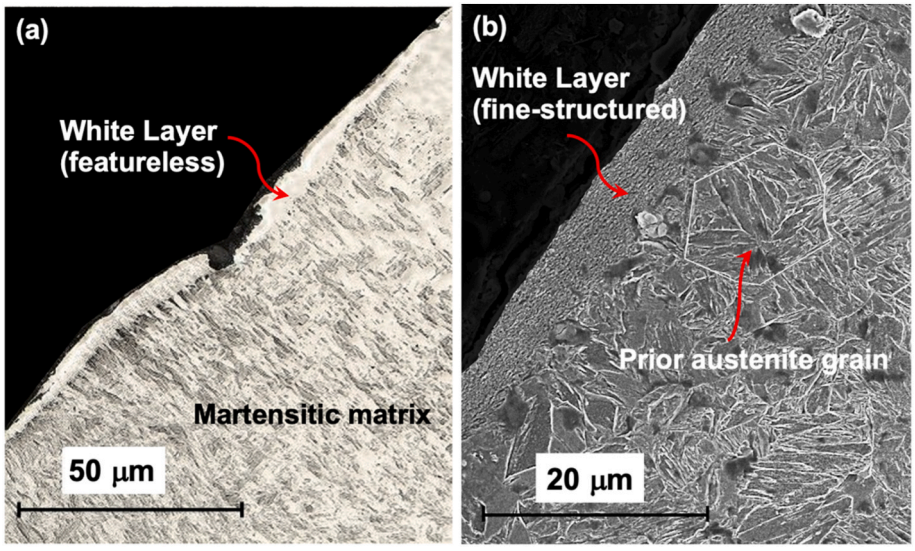

Fig. 4. a) Combined optical and laser scanning confocal image and b) SEM micrograph of the eroded surface (cross-section) indicating the formation of a superficial white layer on the top of the eroded surface and the martensitic microstructure of the bulk material.

and angular particles, WL has been locally cracked, fractured, and in some sections also delaminated. Delamination typically leads to partial material detachment or removal from the surface, as presented in Fig. 4 (a). In a high magnification SEM micrograph in Fig. 4(b), WL is very fine-grained and intensively deformed compared to the underneath and neighboring matrix region. The microhardness of this layer was as high as up to 1270 HV, which was significantly higher than that of the bulk material (~750 HV on average).

Typical martensitic structure can be seen underlying the WL. The induction hardening process before the erosion test resulted in very fine and equiaxed prior austenite grain structure and consequently very fine martensitic features (packets, blocks, and laths). A polygonal prior austenite grain with a diameter of around 15 μm, which comprises of a few fine blocks and packets is marked in Fig. 4(b).

Fig. 5 presents the STEM micrographs along with the corresponding selected area diffraction patterns (SADPs), acquired from sample A and viewed along the [110] zone axis. Fine grains with random crystallographic orientations were detected in the severely deformed WL, as seen in the upper part of Fig. 5(a). Distinct ring patterns are shown in Fig. 5 (b) indicating distorted ultrafine polycrystalline microstructure. Diffraction from many ultrafine grains (through the sample thickness of ~500 nm) with different orientations but the same lattice parameter resulted in producing sharp ring patterns for the topmost part of the FIB sample (WL). Far from the surface and the WL, the neighboring matrix had typical characteristics of lath martensite with a spot-type diffraction pattern for a single martensitic grain orientation, as presented in Fig. 5 (c). According to Fig. 5(a), in this investigated area, the thickness of the nanocrystalline surface layer with nano/ultrafine-grained structure varies between 3 and 5 μm.

Formation mechanism of white layer. The STEM micrographs of the WL structure obtained from sample B along with the corresponding SADP are shown in Fig. 6. According to the microstructure and ring-type SADP, WL is composed of very fine misoriented dislocation cells containing dislocation tangles, where the cell size was detected to be between 50 and 300 nm (in this image) and the overall average being in the order of several hundreds of nanometers. The dislocation cells are

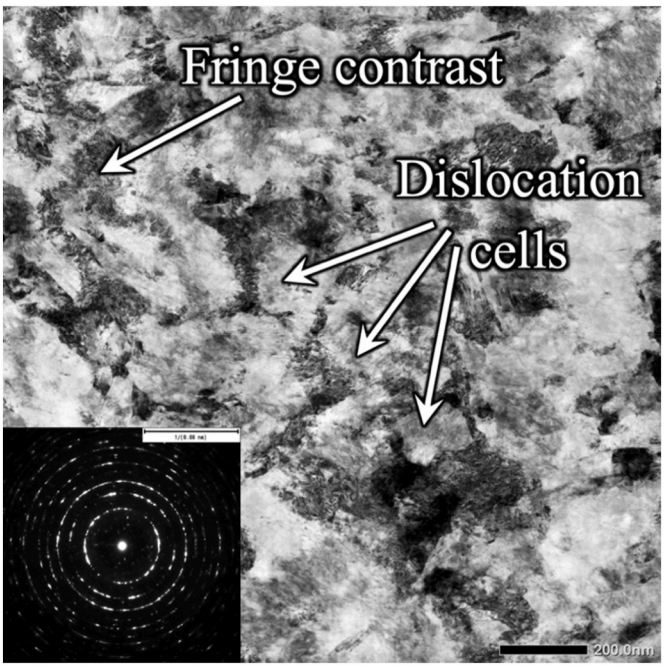

Fig. 6. STEM micrograph of the WL (sample B) and the corresponding SADP showing the dislocation cell-type structure.

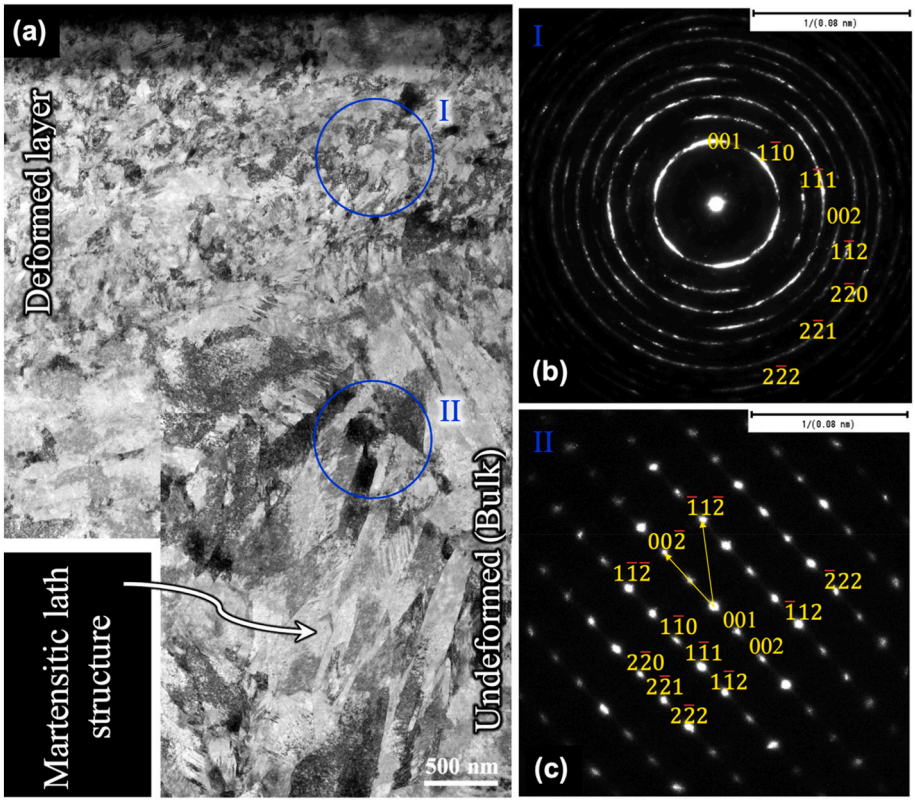

Fig. 5. a) STEM micrographs along with b-c) the corresponding selected area diffraction patterns (SADPs), acquired from the FIB sample A and viewed from the [110] zone axis. b) SADP for the white layer highlighted as region I in Fig. 5(a) and b) SADP for the bulk material highlighted as region II in Fig. 5(a). To cover a larger area and provide sufficient information two STEM images are stitched together in Fig. 5(a).

surrounded by dislocation cell boundaries so that dislocation density inside the cells is relatively lower than those at the boundaries. The formation of the nanoscale dislocation cell-type structure may be attributed to the multidirectional particle impacts and severe plastic deformation in the surface layer. Thus, during the erosion and intense deformation of the surface by solid particle impingements, the movement and rearrangement of dislocations to accommodate the high strain result in this morphology in the topmost of the deformed layer. This kind of cellular structure is reported to be typical in the case of heavily deformed steels [26,29]. It should be noted that several dislocation cells depicted fringe contrast in the STEM micrograph, which can be attributed to nanotwins, stacking faults, the Moire patterns (overlapping of some fine grains/subgrains along with the beam direction), or a combination of them [40,41].

SADP consisted of several clear intense and bright spots, indicating the presence of high angle grain boundaries (HAGBs) as well as many small arcs, indicating the presence of dislocation cell boundaries [29]. During continuous particle impacts, cells may transform into individual subgrains as they must rotate to a certain angle to accommodate further deformation. It is worth noting that no FCC reflections were found in the diffraction patterns of the WL indicating that phase transformation to austenite did not occur during WL formation. The same results were acquired by EBSD. This further supports the hypothesis that enough heat was not generated in the surface layer due to the presence of slurry flow and cooling system and also due to the short contact time between the solid particles and the surface. Moreover, analysis of the chemical composition of the white layers revealed no meaningful difference in the alloying content compared to the bulk material. Hence, high temperature rises or the flash temperature theory proposed by Kuhlmann–Wilsdorf [42] for unlubricated sliding contacts does not play any considerable role on the creation of such structure, here.

For a better illustration, a dark-field (DF) TEM image of the matrix is presented separately in Fig. 7. It reveals formation of several equiaxed or nearly equiaxed nanosized substructures in the range of tens to hundreds of nanometers in the width inside a distinguished martensite block with HAGBs. The misorientation angles across the martensitic block were determined to be high-angle boundaries as marked in orange. According to this DF image, the grains around the orange highlighted boundary have a different zone axis from [110], which strongly suggests that the orange grain boundary is a high-angle boundary. This mechanically-induced ultrafine grain structure seems to be controlled mainly by the activation of different slip systems and the generation of geometrically necessary dislocations. Thus, severe plastic straining may activate different slip system combinations in each individual subgrain. As adjacent misoriented subgrains have their different orientation, they may have different activated slip systems, and to minimize the internal energy of the whole system, a certain common slip system should be selectively activated. As a result, under driving force in the activated common slip systems, the adjacent misoriented subgrains will rotate together to minimize the energy across their boundaries. With further increasing the strain, subgrains that cannot accommodate more deformation (by dislocation gliding) start to rotate separately. Subgrains eventually become highly misoriented grains as rotation angles increase.

As a consequence of the above-mentioned process, severe deformation resulted in restructuring the martensite block so that it has divided into several small components including cells with complex dislocation tangle boundaries, subgrains with low angle grains boundaries (LAGBs), and ultrafine grains with HAGBs. The substructures, which are highlighted with the dashed red lines, showed the same orientation which differed from the orientations of those marked in blue. Thus, it can be assumed that the boundary between cells 1 and 3 and also 6, 7, and 9 are dislocation walls, just with different dislocation densities and spacing. To accommodate plastic straining during the heavy deformation process, dislocation re-arrangement, gliding, interaction, and tangling can initiate the subdivision of martensite blocks. The above-mentioned boundaries, i.e., dislocation cell boundary, HAGB, and LAGBs can be seen in more detail in the high magnification EBSD inverse pole figure map in Fig. 7(b). An alternate and similar image obtained from the EBSD measurement is given in Fig. 8 and **9.** The step size chosen for the scanning was 50 nm. These refined and high resolution EBSD scans made it possible to detect the grain structure and morphology of the white layer.

EBSD image quality along with the grain size distribution of WL as well as the (001) pole figure for the selected area of about 4 μm × 4 μm through the sample thickness of three different regions of WL, interface, and bulk material are presented in Fig. 8. According to EBSD results, extremely fine equiaxed new grains with random crystallographic orientations are observed in the deformed tribological WL so that the grain size was reduced to nanoscale (Fig. 8(a and b) and **9(a, b)**. The grain size distribution inside the WL is plotted in Fig. 8(b). The average grain size was measured to be around 200 nm. As observed in Fig. 8(c), the WL region showed a wide range of random plane direction distribution even in this small area indicating nanocrystalline structure in this layer, whereas along the depth toward the bulk material more specific crystal

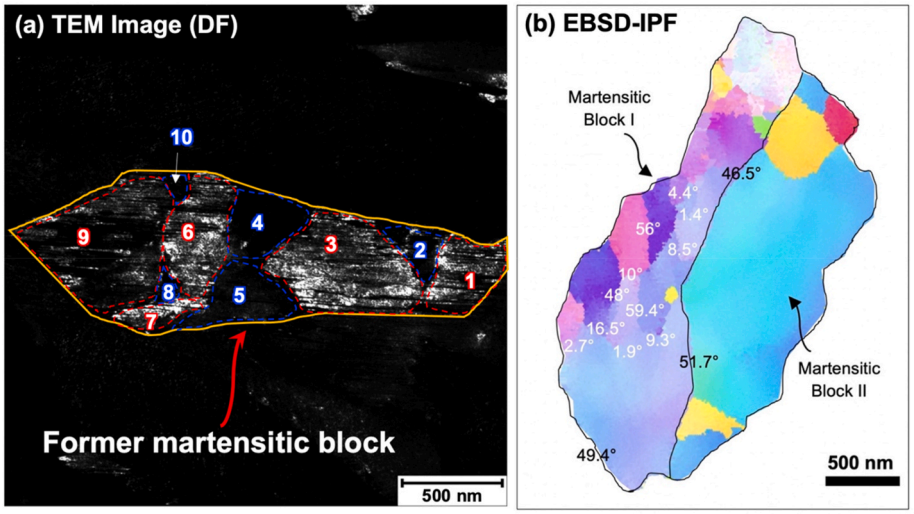

Fig. 7. Formation of dislocation cells inside the prior martensite block obtained from a) TEM dark field image (The cells with almost the same orientation have been numbered with the same color) and b) EBSD inverse pole figure maps of two neighbor blocks. (For interpretation of the references to color in this figure legend, the reader is referred to the Web version of this article.)

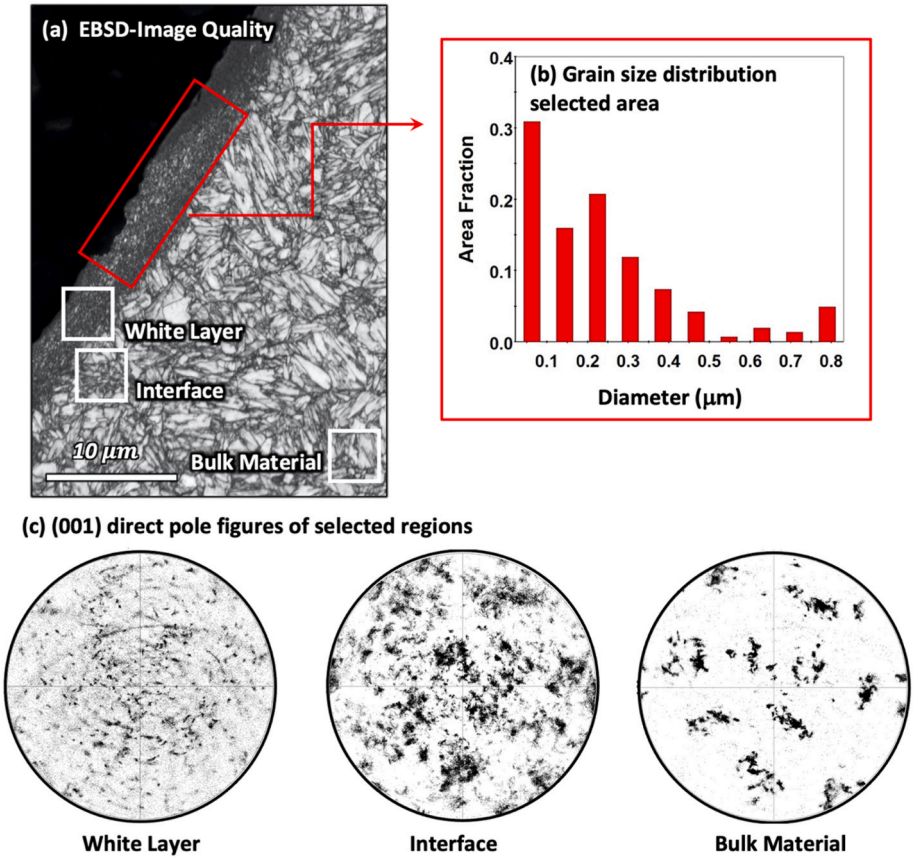

Fig. 8. a) EBSD-Image quality map of eroded sample from an area consisting of WL, bulk material as well as interface region along with b) the grain size distribution of the selected area of WL. c) The (001) pole figures of WL, interface and bulk material obtained from the highlighted areas in Fig. 8(a).

orientations became visible. Fig. 9(c and d) indicate that the fine martensitic blocks have undergone plastic straining to various degrees, leading to the coexistence of dislocation cells, subgrains, and grains. Fig. 9(c) shows two neighboring dislocation cells (denoted by cell 1 and cell 2) in the top right corner. LAGBs and HAGBs are shown in white and black, respectively. Thus, it can be concluded that the grain refinement mechanism and the process of nanocrystalline structure formation started mainly by subdivision of martensite blocks to the dislocation cells and then increasing the misorientations through crystal rotation under further straining. Because of the complex and multi-directional deformation scheme on the surface during slurry erosion, which is consisted of both shear and compressive strains at different rates, no strong texture can be observed in the deformed layer, as expected. In addition, clear subgrain boundaries (white-colored boundaries) can be observed within a large grain with HAGBs (black-colored boundaries). The variations of misorientation angle along the lines I and II shown in Fig. 9(d) confirm the presence of HAGBs and LAGBs, respectively.

The high-speed slurry erosion test using large erosive particles provides high strain, high strain rate, and multi-directional strain path, which effectually promote subgrain rotation and eventually develops high misorientation angles between neighboring subgrains. In fact, the continuous rotation of subgrains to accommodate further strain has resulted in highly misoriented, equiaxed, and ultrafine grains in the order of few hundreds of nanometers. This suggests that the mechanism for the development of high misorientation should be subgrain rotation. The multi-directional particle impacts with the different energies likely affect the activity of various slip systems within a given cell/subgrain depending on the imposed multiaxial stress state, prevailing dislocation densities and associated kinematic hardening effects. Thus, dislocations may not only interact with other dislocations in the current active slip systems but may also interact with inactive dislocations produced in previous deformations caused by the different impact angles. Moreover, when dislocation cell walls have a very high dislocation density and therefore a high slip resistance, further slip activity is likely to focus on areas with lower slip resistance to form new strain localization zones enhancing the grain refinement process. Consequently, further multi-axial deformation can promote refinement of the grain structure when dislocation interactions take place with the existing arrangements. Fig. 10 schematically summarizes the mechanism of the formation of nanocrystalline WL at the martensitic surface layer of the medium-carbon steel.

Modelling of the surface deformation. Single and multiple impact simulations were performed to analyze the deformation behavior of the surface region. The objective of the simulations was to determine the general magnitude of plasticity in the subsurface to shed light on possible deformation conditions leading to the formation of the WL. Fig. 11 shows the equivalent plastic strain (total strain energy of the plastic deformation) after a single, three, and five impacts. The model describes a macroscale response of the material but the effect of crystal structure via crystal plasticity is omitted in this context, and this will be the topic of future research by the same authors team. The particles all impact the small, predetermined region. However, the rock particles encounter a slight shift with respect to each other, and the rocks are also rotated in a different axial orientation. Therefore, different edges of the rocks are in contact with the surface and their subsequent impacts also occur partially in the pre-deformed crater edges. It appeared that the subsurface region generally encounters high plastic strain from 50% up to 80% and the heavily deformed region spreads when the number of impacts increases. The thickness of the extremely deformed layer (e.g., strained to 80%) generally appeared as 15–40 μm. However, even after the first single impact, the surface experienced a high equivalent plastic strain of 50%. Cao et al. [43] considered that the onset of plastic

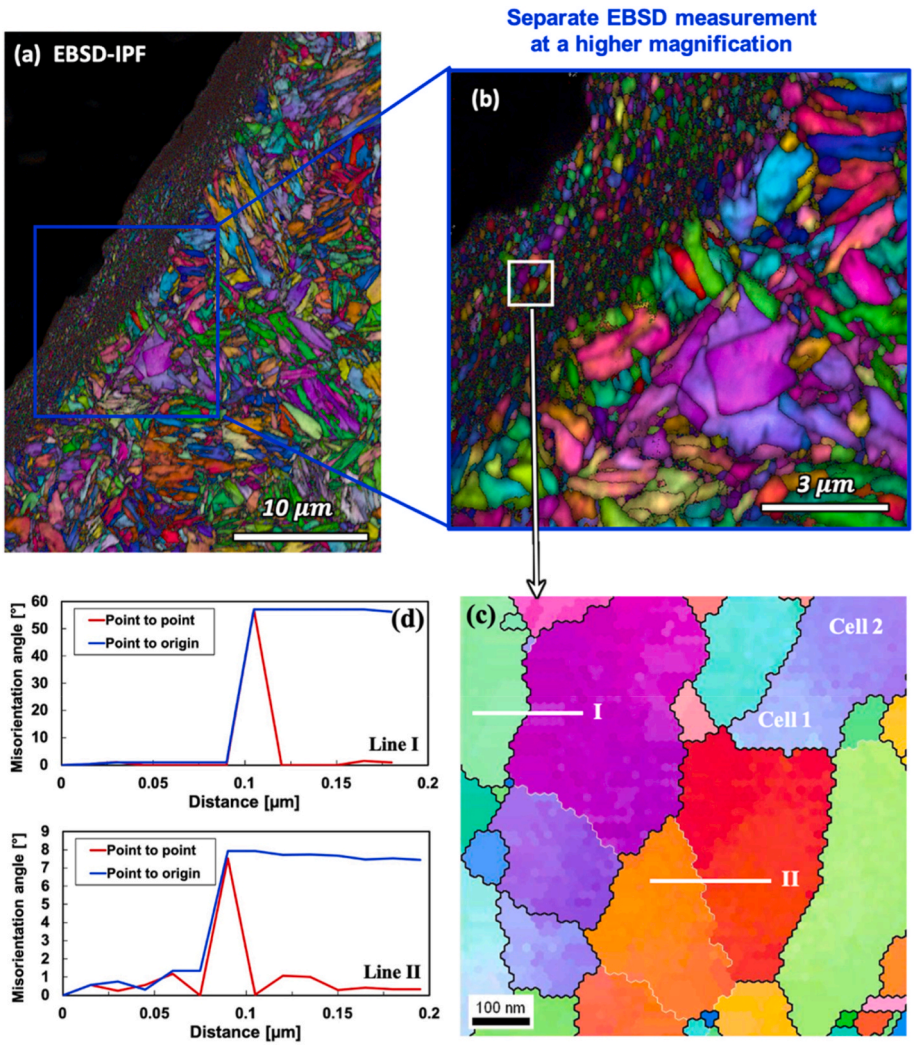

Fig. 9. a) EBSD-inverse pole figure map of an eroded sample from the same area of Fig. 8(a) consisting of WL, bulk material as well as interface region along with b, c) two higher magnification IPF maps of the highlighted areas indicating the structure of WL. d) The misorientation angle distribution along the Line I and Line II marked in Fig. 9(c).

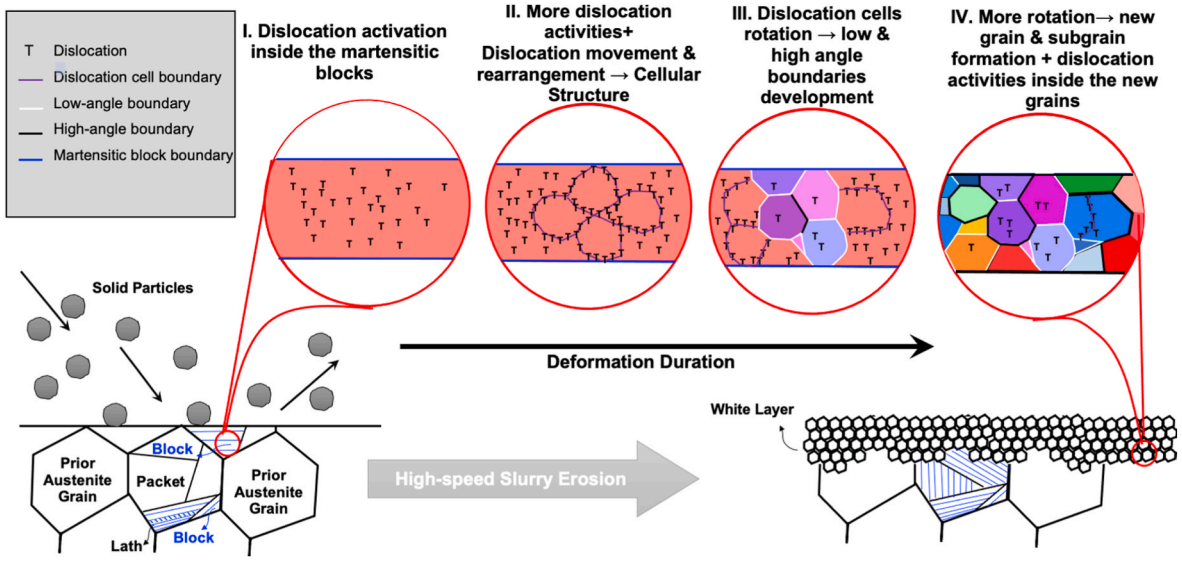

Fig. 10. An illustration for the mechanism of formation of nanocrystalline structure in WL because of the solid particle impacts during the slurry erosion process.

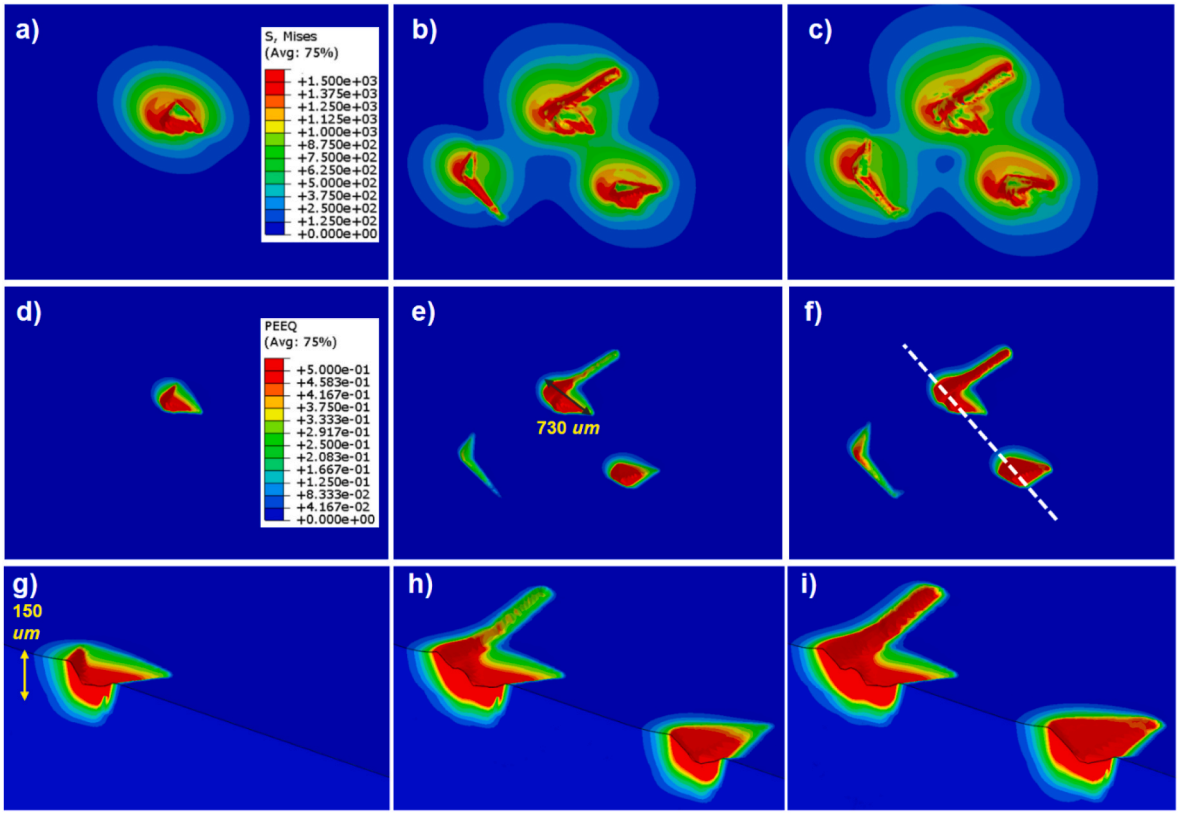

Fig. 11. Von Mises stress (a–c) and equivalent plastic strain distribution (d–i) after a single impact, three impacts, five impacts. Cross-section, shown in (g–i), is marked with a white dashed line on f) and the impact angle is 30°.

deformation can be defined to happen when the equivalent plastic strain reaches a level of 0.2%. The maximum estimated equivalent plastic strain value very close to the surface (after 5 impacts) was around 180%, as shown in Fig. 12, which is in the range of typical severe plastic deformation [44]. Hence, severe plastic deformation can be experienced on the surface even after a few impacts.

The simulations did not aim to reproduce the full loading history of the experiments. However, with the present microstructural observations, it suggests that the level of plastic deformation encountered is sufficient to prescribe feasible conditions for severe local crystal reorientation/substructuring. Frictional heating was not included in the model, but it should be noted that in other cases both adiabatic plasticity-related heating and frictional heating may affect the plastic behavior of the material and cause instantaneous softening. Crystal plasticity can provide more detailed insight to polycrystal level plasticity phenomena, which is a topic of future studies, similarly to what, for example provided for abrasive contacts by the same research team [45]. Especially when finite length scales are investigated, such as 1–100 μm, the macroscale models are close to the limits of continuum approach with macromodeling.

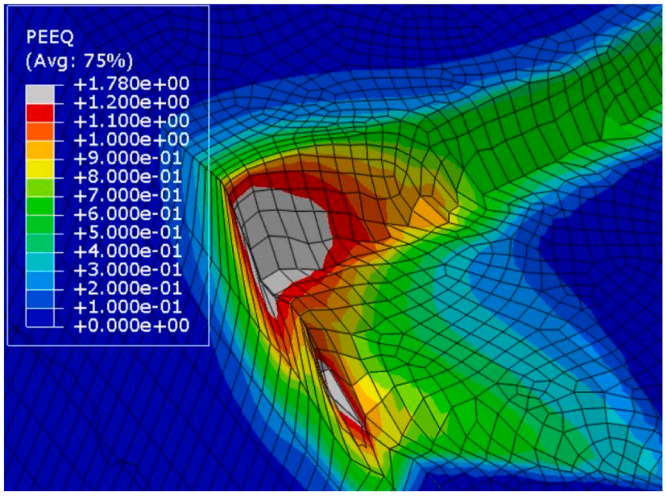

Fig. 12. The maximum equivalent plastic strain on the topmost surface region after five impacts.

Both SEM image of the WL and surrounding areas (Fig. 13(a)) and the modelling results (Fig. 13(b)) show consistently that extensive plastic flow has occurred in the direction of impact, which can introduce enough high number of dislocations inside the surface layer. Later, based on the microstructure observations, further plastic deformation by repetitive solid particle impacts lead to more dislocation activities and eventually leads to local alteration of the structure by the formation of randomly oriented nanograins beneath the impacted surface.

Hardness property of the white layer. Hardness and plastic behavior of the deformed surface (WL) after the slurry erosion test were investigated using nanoindentation experiments and compared to those of the interface and matrix. The load-displacement curves of the WL, interface layer just beneath the WL, and bulk material during nanoindentation measurements are presented in Fig. 14(a). The hardness significantly increased from bulk (5.7 GPa) to the interface region (7.4 GPa, ~30% greater than bulk material) and further to WL (10.1 GPa, ~77% greater than bulk). Furthermore, Fig. 15 shows that the nanohardness and the average grain size of the WL obey the well-known Hall-Petch relationship [46,47]. Here, the average grain size of the WL was determined to be equal to 200 nm, based on both TEM and EBSD examinations. According to Morito et al. [48], amongst the martensitic features, i.e., laths, blocks, and packets, blocks are the key structural parameter in a martensitic microstructure when analyzing the mechanical properties-structure relationship. Thus, the average martensite

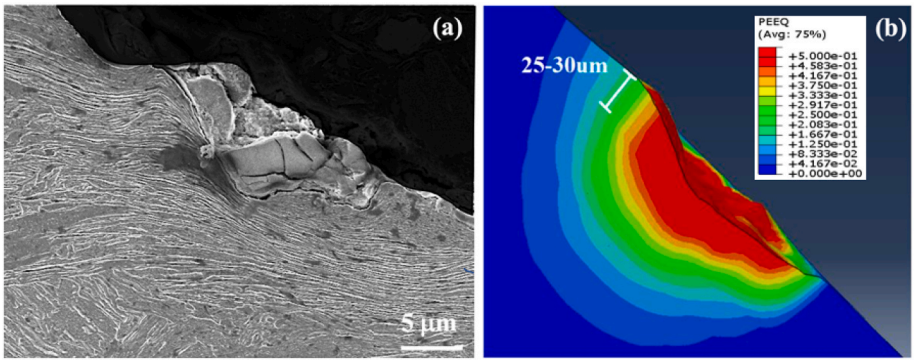

Fig. 13. Two examples of extensive strain and plastic flow as a results of particle impact on the surface. A) SEM image of a cross-sectioned eroded surface and b) a modeling result.

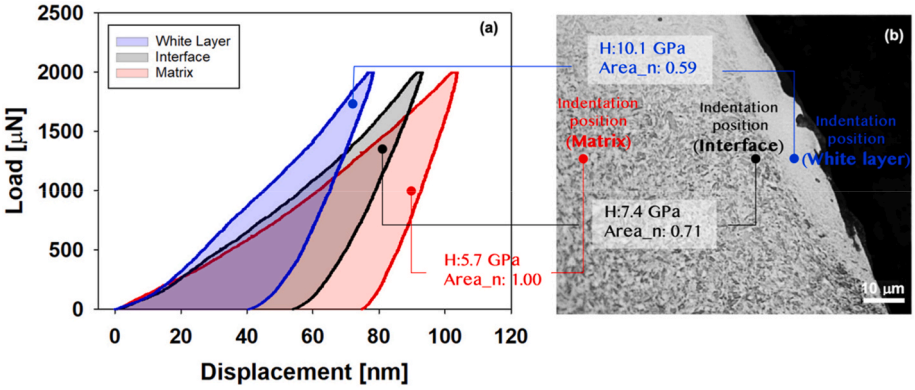

Fig. 14. a) The displacement-load curves of WL, bulk material, and interface region along with b) the hardness value, the ratio of area under each curve to the area under bulk material curve (Area _n) and position of each measurement.

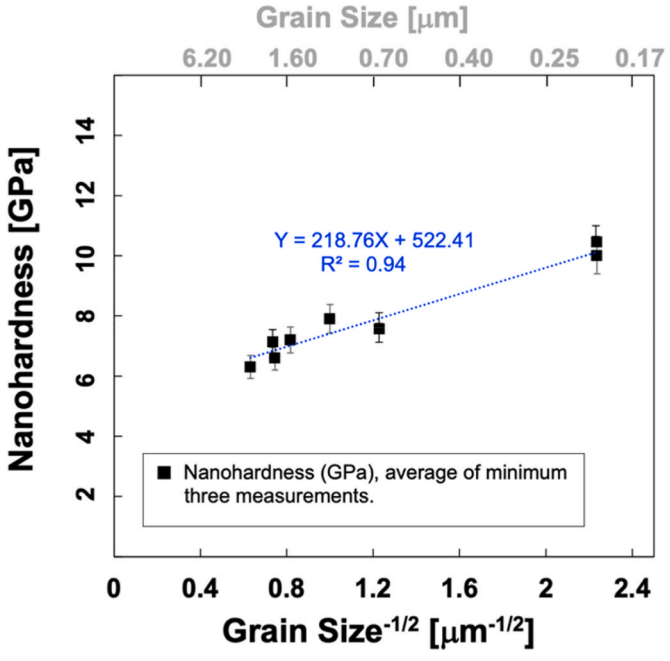

Fig. 15. The relation between the grain size and hardness indicating a typical Hall-Petch behavior.

block size was here considered to be corresponding to the bulk material grain size. To have more data points, the results of other samples (the same composition but different heat treatments), which are not included in this study, were considered for fitting the trend line. A minimum of three measurements at a load of 2 mN were averaged for each condition. Fig. 15 shows an ideal Hall-Petch relationship between the nanohardness values and grain sizes indicating the hardness increment through the grain refinement in the given range. In some studies, hardness of some nanocrystalline structures has been reported to be inconsistent with the Hall-Petch relation due to the high fraction of grain boundaries and hereby the grain boundary weakening effect [46]. However, the grain size softening or inverse Hall-Petch phenomenon is predicted to happen in the grain size range below 100 nm [49], which was not the case in the present study.

Although grain refinement can be considered as the main mechanism of increasing hardness value of WL, some other factors such as increasing the dislocation density, deformation twinning, and deformation kinking can also be expected to affect the WL properties. For the further insight into the WL structure, a bright field (BF) TEM image and corresponding DF and STEM images were captured from a cell-type structured area, as presented in Fig. 16. Clear twinning structure and kink formation can be seen in Fig. 16(a) and (b), respectively. Twinning is often observed at very low strain levels in BCC and HCP alloys in contrast to FCC metals which essentially need certain level of plastic deformation to twin [50,51]. However, all materials can deform predominantly by twinning under shock loading or severe impact conditions [50]. The contribution of nanotwins on the strain hardening of a BCC Ti-alloy under plastic deformation has been well demonstrated by Sadeghpour et al. [52], who also proposed that twin boundaries can act as barriers to further dislocation motion. In addition, deformation kinking is a type of plastic deformation mechanism which is controlled by slip and often occurs as an accommodation mechanism or a stress-relief mechanism during deformation of twins [51,53].

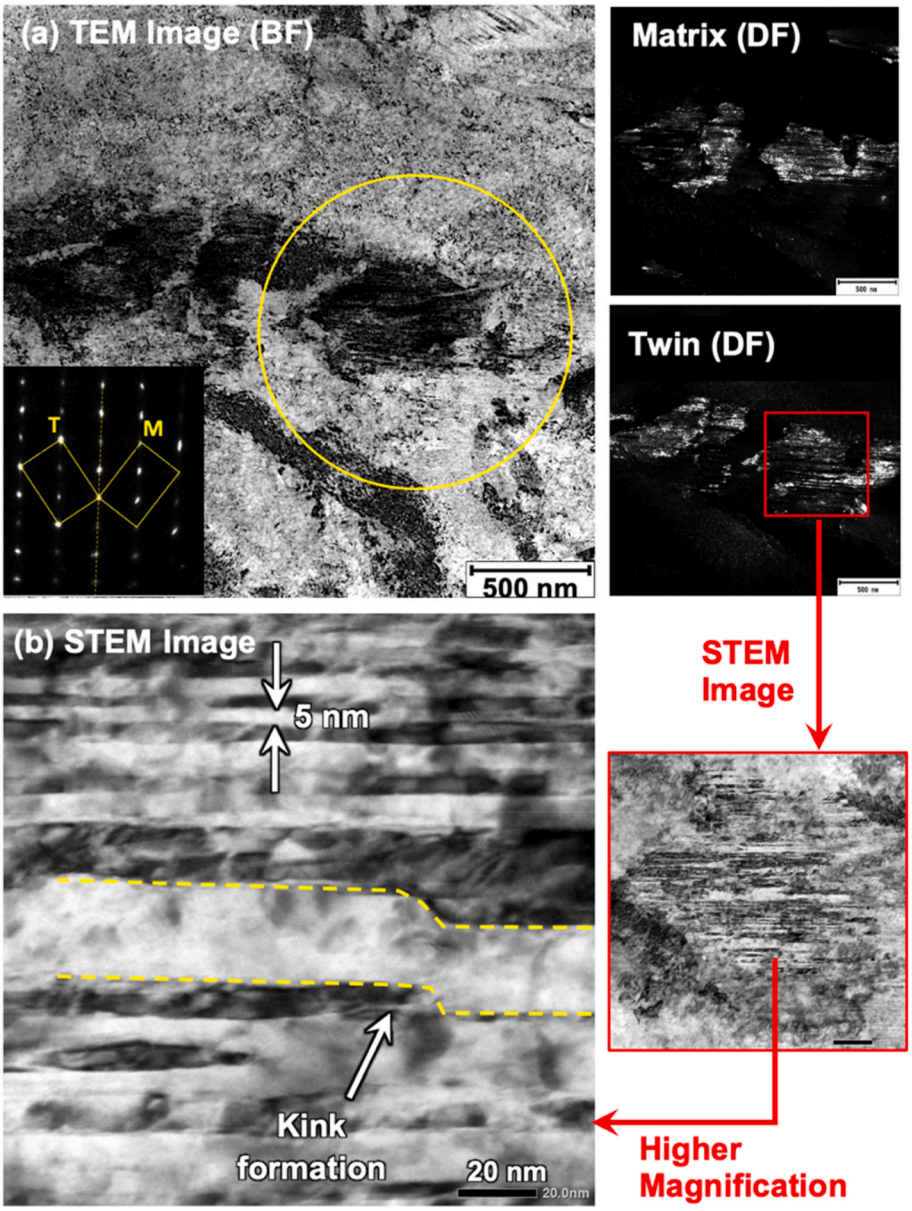

Fig. 16. a) Bright field (BF) TEM micrograph of an individual martensite block in the severely deformed WL. The inset shows the typical twinning diffraction pattern taken from the yellow highlighted region. The corresponding dark field images of M and T (right-hand side images) depict substructure of the matrix and twins. b) High magnification STEM images of the twins inside the nanocrystalline structure and sheared twins creating deformation kinking. (For interpretation of the references to color in this figure legend, the reader is referred to the Web version of this article.)

It should be remarked that in this work both the deformed and undeformed regions consisted of several nanotwins which made it almost impossible to distinguish between the mechanical twins and those formed during the martensite transformation. However, a higher fraction of twins with lower thickness was observed in WL compared to those in the bulk and shearing of the twins was only detected in the WL, such as depicted in Fig. 16(b).

Crack propagation along the interface between the white layer and matrix. It has been already discussed that hardness of the WL can reach an extremely high level thanks to significant grain refinement down to the nano-level as well as due to the high density of dislocations inside the grains. However, such large scale ultra-fine grain formation might lead to deterioration in ductility, potentially leading to spalling and consequently, material loss. The area under the load-displacement curves, reflecting the absorbed energy capacity of the region, is an indication of WL brittleness. Formation and destruction of WL due to the solid particles impact is a progressing phenomenon. WL forms by sever surface deformation and at the same time will be (partly) removed by large and sharp embedded particles and/or by cyclic loading resulting to crack propagation and growth along the interface of the WL and bulk material. One example of this can be seen in Fig. 17. Crack propagation

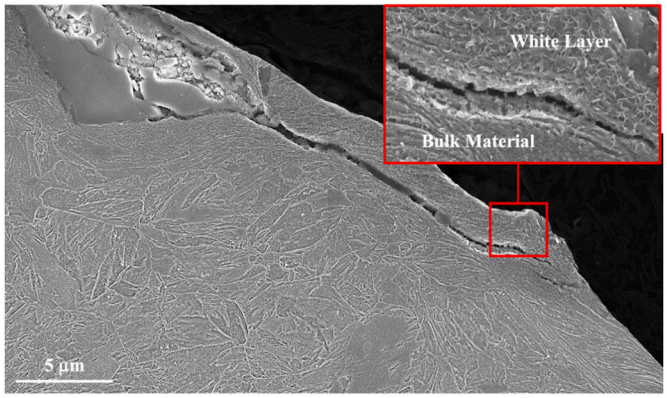

Fig. 17. An example of the cross-section of the surface damaged. Crack is initiated by an embedded particle and then propagated along the interface of the WL and bulk material (FESEM image).

within the WL, giving evidence of its high brittleness, appears to be terminated when the crack comes into contact with the base material, or otherwise, cracks propagate along the interface. In this instance, it seems that a crack has formed in the WL, which has then chipped away (spalled) from the bulk.

Regarding the effect of WL on the erosion behavior, the fine-structured WL showed a 77% higher hardness level than that of the bulk material which can enhance the erosion resistance of the surface. On the other hand, the nanohardness results along with the eroded surface imaging indicated that WL is genuinely brittle compared to the bulk (40% less capacity to absorb the impact energy), which promotes large material delamination and removal from the surface and consequently, deteriorate the erosion performance. In other words, WL can be consistently and repeatedly created, removed, and recreated on and from the surfaces. Hence, the total mass loss depends on the thickness as well as the endurance and stability of WL against the heavy particles' impact, abrasion, and surface fatigue. It is worth mentioning that the presented experimental results are after the given test duration and the properties and thickness of the WL may differ with the test time.

Modelling results revealed that severe plastic strains can occur even after very few impacts. They confirm that WL formation during the slurry erosion condition preset in this work can be intrinsically linked to the presence of high plastic strains. The model should be improved to be able to help formulating a balance between WL formation and destruction in favor of improving the erosion performance by including the crystal plasticity, work hardening effect as well as considering the multi-directional impacts in order to reach the optimum process parameters, especially particle size and velocity. The ideal condition would be having a very shallow and superficial WL to act as surface protection. Such that the magnitude of material removal just because of the WL is minimum. Moreover, the cell structure seems to be formed inside the martensitic block indicating that the size of blocks can also control the WL formation, which can be also the topic of future research.

4. Conclusions

In this work, extensive microstructural investigations were performed to characterize and to a better understanding of extremely deformed surface layer, called ''white layer'', formed in a medium-carbon martensitic steel after being subjected to 10–12 mm solid particle impacts during high-speed slurry erosion pot test. On the basis of the presented results and analyses the following conclusions are drawn:

- The slurry erosion process can introduce a nanocrystalline structure in the surface layer (white layer) with a nano/ultrafine grain distribution with an average size of 200 nm, as revealed with EBSD and TEM investigations.
- The thickness of the white layer varies between 3 and 10 μm in the investigated microstructures.
- The mechanically induced formation of white layer due to severe plastic deformation on the surface is the predominant mechanism. No evidence of phase transformation during formation of this layer was observed.
- The nanohardness level of white layer can extremely increase (around +77%), presumably mainly due to the grain refinement mechanism. Typical Hall-Petch correlation between the hardness and size of the grains in both white layer and bulk material exists.
- Micrograph of the cracked surface along with nanohardness analysis indicate to the brittleness of white layer compared to lath-type martensitic bulk material.
- The surface layer can experience a high strain level, which can develop the observed microstructural changes in white layer, as revealed by the modelling results.

Declaration of competing interest

The authors declare that they have no known competing financial interests or personal relationships that could have appeared to influence the work reported in this paper.

Acknowledgments

The authors are grateful for the financial support from the Academy of Finland (#311934 – Genome of Steel Project). The corresponding author would also like to thank Jenny and Antti Wihuri Foundation for the financial support.

References

[1] S. Akcan, W.S. Shah, S.P. Moylan, S. Chandrasekar, P.N. Chhabra, H.T.Y. Yang, Formation of white layers in steels by machining and their characteristics, Metall. Mater. Trans. A. 33 (2002) 1245–1254, https://doi.org/10.1007/s11661-002-0225-z.

[2] W.J. Tomlinson, L.A. Blunt, S. Spraggett, White Layers on surface of ground EN24 Steel: 1 microstructure, composition, internal Sstress, and corrosion properties, Surf. Eng. 5 (1989) 229–234, https://doi.org/10.1179/sur.1989.5.3.229.

[3] D. Turley, The nature of the white-etching surface layers produced during reaming ultra-high strength steel, Mater. Sci. Eng. 19 (1975) 79–86, https://doi.org/10.1016/0025-5416(75)90010-5.

[4] A. Barbacki, M. Kawalec, A. Hamrol, Turning and grinding as a source of microstructural changes in the surface layer of hardened steel, J. Mater. Process. Technol. 133 (2003) 21–25, https://doi.org/10.1016/S0924-0136(02)00211-X.

[5] S.B. Hosseini, U. Klement, A descriptive phenomenological model for white layer formation in hard turning of AISI 52100 bearing steel, CIRP J. Manuf. Sci. Technol. 32 (2021) 299–310, https://doi.org/10.1016/j.cirpj.2021.01.014.

[6] Y.K. Chou, C.J. Evans, White layers and thermal modeling of hard turned surfaces, Int. J. Mach. Tool Manufact. 39 (1999) 1863–1881, https://doi.org/10.1016/S0890-6955(99)00036-X.

[7] A. Aramcharoen, P.T. Mativenga, White layer formation and hardening effects in hard turning of H13 tool steel with CrTiAlN and CrTiAlN/MoST-coated carbide tools, Int. J. Adv. Manuf. Technol. 36 (2008) 650–657, https://doi.org/10.1007/s00170-006-0899-2.

[8] S.S. Bosheh, P.T. Mativenga, White layer formation in hard turning of H13 tool steel at high cutting speeds using CBN tooling, Int. J. Mach. Tool Manufact. 46 (2006) 225–233, https://doi.org/10.1016/j.ijmachtools.2005.04.009.

[9] Y.Y. Yang, H.S. Fang, W.G. Huang, A study on wear resistance of the white layer, Tribol. Int. 29 (1996) 425–428, https://doi.org/10.1016/0301-679X(95)00099-.

[10] V. Javaheri, D. Porter, V.T. Kuokkala, Slurry erosion of steel – review of tests, mechanisms and materials, Wear 408–409 (2018) 248–273, https://doi.org/10.1016/j.wear.2018.05.010.

[11] N. Ojala, K. Valtonen, A. Antikainen, A. Kemppainen, J. Minkkinen, O. Oja, V. Kuokkala, Wear performance of quenched wear resistant steels in abrasive slurry erosion, Wear 354–355 (2016) 21–31, https://doi.org/10.1016/j.wear.2016.02.019.

[12] V. Ratia, Behavior of Martensitic Wear Resistant Steels in Abrasion and Impact Wear Testing Conditions, Tampere University of Technology, 2015. https://trepo.tuni.fi//handle/10024/113966.

[13] B. Zhang, W. Shen, Y. Liu, X. Tang, Y. Wang, Microstructures of surface white layer and internal white adiabatic shear band, Wear 211 (1997) 164–168, https://doi.org/10.1016/S0043-1648(97)00099-9.

[14] D.H. Cho, S.A. Lee, Y.Z. Lee, Mechanical properties and wear behavior of the white layer, Tribol. Lett. 45 (2012) 123–129, https://doi.org/10.1007/s11249-011-9869-4.

[15] E. Sauger, L. Ponsonnet, J. Martin, L. Vincent, Study of the tribologically transformed structure created during fretting tests, Tribol. Int. 33 (2000) 743–750, https://doi.org/10.1016/S0301-679X(00)00088-8.

[16] D.A. Rigney, L.H. Chen, M.G.S. Naylor, A.R. Rosenfield, Wear processes in sliding systems, Wear 100 (1984) 195–219, https://doi.org/10.1016/0043-1648(84)90013-9.

[17] M. Busquet, S. Descartes, Y. Berthier, Formation conditions of mechanically modified superficial structures for two steels, Tribol. Int. 42 (2009) 1730–1743, https://doi.org/10.1016/j.triboint.2009.04.045.

[18] J.E. Morgan, Structural and microstructural changes in the inner races of ball bearings, Wear 84 (1983) 51–64, https://doi.org/10.1016/0043-1648(83)90118-7.

[19] J. Barry, G. Byrne, TEM study on the surface white layer in two turned hardened steels, Mater. Sci. Eng. A. 325 (2002) 356–364, https://doi.org/10.1016/S0921-5093(01)01447-2.

[20] O. Haiko, V. Javaheri, K. Valtonen, A. Kaijalainen, J. Hannula, Effect of Prior Austenite Grain Size on the Abrasive Wear Resistance of Ultra-high Strength Martensitic Steels, vol. 455, 2020, pp. 13–16, https://doi.org/10.1016/j.wear.2020.203336.

[21] T. Sakai, H. Miura, X. Yang, Ultrafine grain formation in face centered cubic metals during severe plastic deformation, Mater. Sci. Eng. A. 499 (2009) 2–6, https://doi.org/10.1016/j.msea.2007.11.098.

[22] C. Figueroa, R. Schouwenaars, V. Jacobo, A. Ortiz, R. Petrov, L. Kestens, Tribological and microstructural characterization of ultrafine layers induced by wear in ductile alloys, Tribol. Online 11 (2016) 389–395, https://doi.org/10.2474/trol.11.389.
[23] J. Schöfer, P. Rehbein, U. Stolz, D. Löhe, K.-H. Zum Gahr, Formation of tribochemical films and white layers on self-mated bearing steel surfaces in boundary lubricated sliding contact, Wear 248 (2001) 7–15, https://doi.org/10.1016/S0043-1648(00)00549-4.
[24] R. Hossain, F. Pahlevani, V. Sahajwalla, Revealing the mechanism of extraordinary hardness without compensating the toughness in a low alloyed high carbon steel, Sci. Rep. 10 (2020) 181, https://doi.org/10.1038/s41598-019-55803-6.
[25] V. Javaheri, O. Haiko, S. Sadeghpour, K. Valtonen, J. Kömi, D. Porter, On the role of grain size on slurry erosion behavior of a novel medium-carbon, low-alloy pipeline steel after induction hardening, Wear (2021) 203678, https://doi.org/10.1016/j.wear.2021.203678.
[26] D.H. Shin, I. Kim, J. Kim, K.-T. Park, Grain refinement mechanism during equal-channel angular pressing of a low-carbon steel, Acta Mater. 49 (2001) 1285–1292, https://doi.org/10.1016/S1359-6454(01)00010-6.
[27] M. Mohammadnezhad, M. Shamanian, A. Zabolian, M. Taheri, V. Javaheri, A. H. Navidpour, M. Nezakat, J.A. Szpunar, Microstructure and crystallographic texture variations in the friction-stir-welded al-al2o3-b4c metal matrix composite produced by accumulative roll bonding, Metall. Mater. Trans. A Phys. Metall. Mater. Sci. 46 (2015) 5747–35755, https://doi.org/10.1007/s11661-015-3139-2.
[28] S. Lu, Z. Wang, K. Lu, Strain-induced microstructure refinement in a tool steel subjected to surface mechanical attrition treatment, J. Mater. Sci. Technol. 26 (2010) 258–263, https://doi.org/10.1016/S1005-0302(10)60043-6.
[29] R.D.K. Misra, Z. Zhang, P.K.C. Venkatasurya, M.C. Somani, L.P. Karjalainen, Martensite shear phase reversion-induced nanograined/ultrafine-grained Fe–16Cr–10Ni alloy: the effect of interstitial alloying elements and degree of austenite stability on phase reversion, Mater. Sci. Eng. A. 527 (2010) 7779–7792, https://doi.org/10.1016/j.msea.2010.08.051.
[30] N.R. Tao, M.L. Sui, J. Lu, K. Lua, Surface nanocrystallization of iron induced by ultrasonic shot peening, Nanostruct. Mater. 11 (1999) 433–440, https://doi.org/10.1016/S0965-9773(99)00324-4.
[31] K. Valtonen, N. Ojala, O. Haiko, V. Kuokkala, Comparison of various high-stress wear conditions and wear performance of martensitic steels, Wear 426–427 (2019) 3–13, https://doi.org/10.1016/j.wear.2018.12.006.
[32] O. Haiko, K. Valtonen, A. Kaijalainen, S. Uusikallio, J. Hannula, T. Liimatainen, J. Kömi, Effect of tempering on the impact-abrasive and abrasive wear resistance of ultra-high strength steels, Wear 440–441 (2019) 203098, https://doi.org/10.1016/j.wear.2019.203098.
[33] V. Javaheri, J.I. Asperheim, B. Grande, S. Kolli, D. Porter, Simulation and experimental studies of induction hardening behavior of a new medium-carbon, low-alloy wear resistance steel, COMPEL - Int. J. Comput. Math. Electr. Electron. Eng. 39 (2019) 158–165, https://doi.org/10.1108/COMPEL-06-2019-0227.
[34] V. Javaheri, S. Pallaspuro, A. Kaijalainen, S. Sadeghpour, J. Kömi, D. Porter, Promising bending properties of a new as-rolled medium-carbon steel achieved with furnace-cooled bainitic microstructures, Mater. Sci. Eng. A. 796 (2020) 140011, https://doi.org/10.1016/j.msea.2020.140011.
[35] V. Javaheri, A. Pohjonen, J.I. Asperheim, D. Ivanov, D. Porter, Physically based modeling, characterization and design of an induction hardening process for a new slurry pipeline steel, Mater. Des. 182 (2019) 108047, https://doi.org/10.1016/j.matdes.2019.108047.
[36] V. Javaheri, T. Nyyssönen, B. Grande, D. Porter, Computational design of a novel medium-carbon, low-alloy steel microalloyed with niobium, J. Mater. Eng. Perform. 27 (2018), https://doi.org/10.1007/s11665-018-3376-9, 2978–32992.
[37] V. Javaheri, N. Khodaie, A. Kaijalainen, D. Porter, Effect of niobium and phase transformation temperature on the microstructure and texture of a novel 0.40% C thermomechanically processed steel, Mater. Char. 142 (2018) 295–308, https://doi.org/10.1016/j.matchar.2018.05.056.
[38] N. Ojala, K. Valtonen, P. Kivikytö-Reponen, P. Vuorinen, P. Siitonen, V.-T. Kuokkala, Effect of test parameters on large particle high speed slurry erosion testing, Tribol. Mater. Surface Interfac. 8 (2014) 98–104, https://doi.org/10.1179/1751584X14Y.0000000066.
[39] M. Lindroos, M. Apostol, V.-T. Kuokkala, A. Laukkanen, K. Valtonen, K. Holmberg, O. Oja, Experimental study on the behavior of wear resistant steels under high velocity single particle impacts, Int. J. Impact Eng. 78 (2015) 114–127, https://doi.org/10.1016/j.ijimpeng.2014.12.002.
[40] J. Tu, TEM nano-moiré pattern analysis of a copper/single walled carbon nanotube nanocomposite synthesized by laser surface implanting, Chimia 4 (2018) 19, https://doi.org/10.3390/c4010019.
[41] J. Kong, M. Sabatini, L. Monaco, J. Tam, J.L. McCrea, G. Palumbo, J. Howe, U. Erb, Characterization of a nanocrystalline NiCo electroformed sheet metal, J. Mater. Sci. 56 (2021) 1749–1767, https://doi.org/10.1007/s10853-020-05325-8.
[42] D. Kuhlmann-Wilsdorf, Temperatures at interfacial contact spots: dependence on velocity and on role reversal of two materials in sliding contact, J. Tribol. 109 (1987) 321–329, https://doi.org/10.1115/1.3261361.
[43] S.C. Cao, X. Zhang, J. Lu, Y. Wang, S.-Q. Shi, R.O. Ritchie, Predicting surface deformation during mechanical attrition of metallic alloys, Npj Comput. Mater. 5 (2019) 36, https://doi.org/10.1038/s41524-019-0171-6.
[44] V. Segal, Review: modes and processes of pevere plastic deformation (SPD), Materials 11 (2018) 1175, https://doi.org/10.3390/ma11071175.
[45] M. Lindroos, A. Laukkanen, T. Andersson, Micromechanical modeling of polycrystalline high manganese austenitic steel subjected to abrasive contact, Friction 8 (2020) 626–642, https://doi.org/10.1007/s40544-019-0315-1.
[46] S.N. Naik, S.M. Walley, The Hall–Petch and inverse Hall–Petch relations and the hardness of nanocrystalline metals, J. Mater. Sci. 55 (2020) 2661–2681, https://doi.org/10.1007/s10853-019-04160-w.
[47] N.J. Petch, The cleavage strength of polycrystals, J. Iron Steel Inst. 174 (1953) 25–28.
[48] S. Morito, H. Yoshida, T. Maki, X. Huang, Effect of block size on the strength of lath martensite in low carbon steels, Mater. Sci. Eng. A. 438–440 (2006) 237–240, https://doi.org/10.1016/j.msea.2005.12.048.
[49] D.A. Konstantinidis, E.C. Aifantis, On the “Anomalous” hardness of nanocrystalline materials, Nanostruct. Mater. 10 (1998) 1111–1118, https://doi.org/10.1016/S0965-9773(98)00145-7.
[50] D. Zhang, L. Jiang, B. Zheng, J.M. Schoenung, S. Mahajan, E.J. Lavernia, I. J. Beyerlein, J.M. Schoenung, E.J. Lavernia, Deformation twinning (update), in: Ref. Modul. Mater. Sci. Mater. Eng, Elsevier, 2016, https://doi.org/10.1016/B978-0-12-803581-8.02878-2.
[51] S. Sadeghpour, S.M. Abbasi, M. Morakabati, L.P. Karjalainen, Effect of dislocation channeling and kink band formation on enhanced tensile properties of a new beta Ti alloy, J. Alloys Compd. 808 (2019) 151741, https://doi.org/10.1016/j.jallcom.2019.151741.
[52] S. Sadeghpour, S.M. Abbasi, M. Morakabati, A. Kisko, L.P. Karjalainen, D.A. Porter, A new multi-element beta titanium alloy with a high yield strength exhibiting transformation and twinning induced plasticity effects, Scripta Mater. 145 (2018) 104–108, https://doi.org/10.1016/j.scriptamat.2017.10.017.
[53] M. Eskandari, M.A. Mohtadi-Bonab, A. Zarei-Hanzaki, J.A. Szpunar, L. P. Karjalainen, EBSD Study of deformation microstructure of an as-homogenized austenitic mn steel after hot compression, Adv. Eng. Mater. 20 (2018) 1800327, https://doi.org/10.1002/adem.201800327.